Journal of Materials Chemistry C

ROYAL SOCIETY OF CHEMISTRY

PAPER

View Article Online
View Journal | View Issue



Cite this: J. Mater. Chem. C, 2023, 11, 11671

# Supramolecular polymerization of chiral platinum(II) complexes: transformable nanoassemblies and their amplified circularly polarized luminescence†

Xiaolin Zhu, *‡ Zhen Wang,‡ Yihui Jia, Fang Yang, Youzhi Zhang, Shirui Zhao and Xiaoming He *

Received 6th July 2023,
Accepted 3rd August 2023

DOI: 10.1039/d3tc02375c

rsc.li/materials-c

Herein, we report four pairs of enantiomeric platinum(II) complexes **D/L-Pt-1–Pt-4** with minor structural variations that have been found to lead to distinct self-assembly behaviors and form various well-defined nanostructures. Notably, **Pt-1** exhibits polymorphic self-assembly with well-defined nanostructures, such as nanorings, nanotwists, dendritic twists, and microbelts, in various conditions through the interplay of different non-covalent interactions. Importantly, two pairs of enantiomers **D/L-Pt-1–Pt-2** show significantly amplified effects for circular dichroism (CD) and circularly polarized luminescence (CPL) in their corresponding nanoassemblies. Moreover, the self-assembly process can be governed by the Pt···Pt/π–π stacking, the solvophobic interactions, and electrostatic repulsion provided by the positively charged tridentate cyclometalated platinum(II) moieties. The detailed supramolecular polymerization pathway was systematically investigated by spectroscopy, X-ray single-crystal diffraction, and electron microscopy studies.



*Key Laboratory of Applied Surface and Colloid Chemistry (Ministry of Education), School of Chemistry and Chemical Engineering, Shaanxi Normal University, Xi'an 710119, P. R. China. E-mail: xiaolinchem@snnu.edu.cn*

† Electronic supplementary information (ESI) available: Detailed experimental procedures; crystals data for ligands; detailed structural characterization data, crystal data, DFT calculations, and photophysical studies. CCDC 2209733, 2209735 and 2209736. For ESI and crystallographic data in CIF or other electronic format see DOI: https://doi.org/10.1039/d3tc02375c

‡ These authors contributed equally.

**Xiaolin Zhu**

*Dr Xiaolin Zhu is an Associate Professor at the Shaanxi Normal University from Dec. 2019. He received his BSc degree and PhD degree from Nanjing Tech University. After graduation, he worked as a postdoc fellow at North Dakota State University, New Jersey Institute of Technology, and San Diego State University. His research interests focus on the study of optoelectronic properties of supramolecular photofunctional materials and their applications in photocatalysis.*

## Introduction

The spontaneous self-assembly of molecules through non-covalent interactions into dynamically elongated nanoarchitectures has attracted considerable interest over the past few decades owing to their potential applications in the fields of materials and life sciences.[1–11] Supramolecular polymerizations have been mainly built from purely organic building blocks since the first report in 1990.[11] There has been a notable advance in the understanding of the formation process of supramolecular polymerizations,[8–10] which are primarily driven by the combination of various non-covalent interactions, including π–π stacking, hydrogen bonding, electrostatic, and hydrophobic–hydrophobic interactions.[10–13] Inspired by the coordination polymers, the incorporation of metal centers, in particular, $d^8$ and $d^{10}$ transition metals, into systems has enabled the self-assemblies novel topological structures and interesting luminescence properties due to the presence of additional metal–metal interactions in transition metal complexes.[14,15]

Among the $d^8$ and $d^{10}$ transition metal complexes, square-planar $d^8$ platinum(II) complexes have been extensively explored owing to their propensity to self-assemble into ordered nanostructures, driven by metal–metal and/or π–π stacking interactions.[14–18] In addition, the Pt(II) complexes possess rich photophysical properties, such as intense absorption in the

visible region and drastic color and emission changes during the process of self-assembly.[18–20] These unique properties make Pt(II) complexes promising candidates for a variety of optoelectronic and biomedical applications, including organic light-emitting devices (OLEDs), photocatalysis, molecular recognition, biological imaging, and nonlinear optics.[15–22] In this regard, Pt(II) complexes have been recognized as ideal small molecules to construct a wide variety of supramolecular nanomaterials. More importantly, controlling the topological structures of biological polymers, such as protein folding/unfolded process, plays a crucial role in a biological system.[8,12,13] However, the ability of multiple assembly pathways for the same monomer may lead to the formation of various aggregates with distinct molecular packing, optical properties, and thermodynamic stability, depending closely on the self-assembly conditions, which is a fundamental challenge for researchers.[2,14] To obtain the desired self-assemblies, mechanistic insights into the complex pathways and control of the kinetic effects are essential.[23] It has been demonstrated that the formation of assembly aggregates can be affected by kinetically trapped or metastable aggregates that compete with thermodynamically stable states.[24–27] For example, Würthner *et al.* have developed a series of fluorescent supramolecular systems of perylene bisimide-based J-aggregates, in which kinetically trapped states are directed by imide hydrogen-bonding interactions.[2,28] Recently, Fernández *et al.* have demonstrated the strategy of N–H···Cl–$M^{II}$ interactions in controlling kinetic pathways for the self-assembly of imide-substituted bispyridyldihalogen $Pt^{II}$/$Pd^{II}$ complexes.[14,29–31] We recently reported two pyrazole-based kinetically trapped BODIPY dyes that exhibited self-assembly behavior and competing pathways to form metastable J-aggregates and thermodynamically stable H-aggregates.[32] Nevertheless, well-documented examples of "kinetically trapped" supramolecular polymerization for Pt(II) complexes are scarce. Thus, the development of a single Pt(II) complex that involves more than two different assemblies with distinct optical and morphological properties is highly required.

Our previous studies reported a series of Pt(II) isocyanide complexes bearing amide linkers that exhibited cooperative supramolecular polymerization in non-polar solvents, whereas isodesmic self-assembly for Pt(II) complexes with ester linkers.[33] Based on these results, the class of Pt(II) complexes might have the possibility to self-assemble two or even more different assemblies with distinct properties by controlling kinetic effects. To explore this point, herein we have designed two enantiomeric pairs of chiral organoplatinum(II) complexes **D/L-Pt-1**, and **D/L-Pt-2**, which bear two different chiral isocyanide ligands (Scheme 1). To minimize the structural variations, two similar chiral camphorone-based isocyanides with considerable steric hindrance were chosen as the auxiliary ligands, with two different linking groups, *i.e.* amide or methylene sulfonamide. Their supramolecular polymerization behaviors, associated with photophysical changes in various solvents and their other well-defined nanostructures, have been systematically investigated.

The motivations of the molecular design are as follows: (1) the pincer C^N^N ligands and substituted aromatic isocyanide ligands not only can promote the self-assembly process by intermolecular π–π interactions, but also are beneficial for the spectroscopic analysis of the self-assembled process. (2) The type of the linker seems to determine the pathway complexity: for complex **Pt-2** with methylene sulfonamide as the linker, intermolecular hydrogen bonding between the carboxyl groups and N–H can efficiently occur for complex **Pt-2** in a nonpolar solvent, resulting in thermodynamically controlled assemblies. In contrast, the utilization of an amide group as the linker,

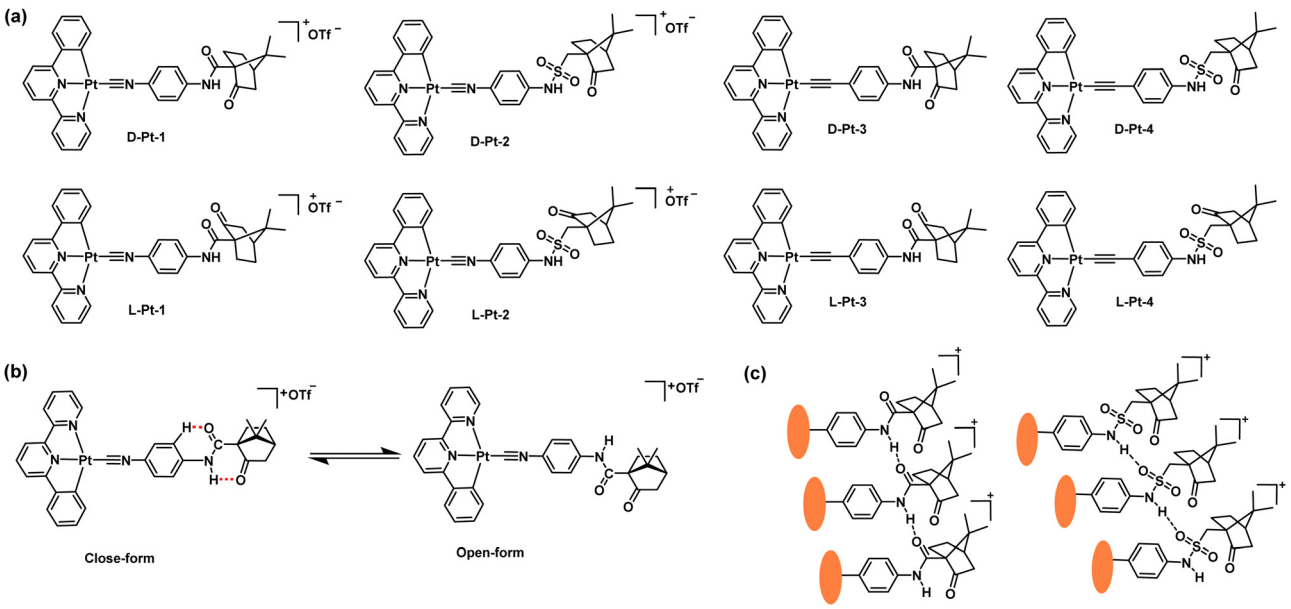


Scheme 1 (a) Molecular structures of platinum(II) complexes **D/L-Pt-1–Pt-4**; (b) the chemical equilibrium between the open and close conformations; (c) the proposed intermolecular hydrogen bonding packing mode for **Pt-1** and **Pt-2**.

 

together with a carbonyl group on camphorone, allows the formation of an intramolecularly H-bonded pseudocycle for complex **Pt-1** (Scheme 1), giving an equilibrium co-existence of the ''closed-form'' and ''open-form'' monomeric species in the solution. Initially, the solvophobic interactions together with Pt···Pt and π–π interactions drive the self-assembly of complex **Pt-1** into metastable nanotoroids. Over time, steric hindrance effects induce a molecular rearrangement into flexible nanofibers, including nanotwists and nanohelixes, that are stabilized by intermolecular hydrogen bonding of amide and carbonyl groups. The final formation of microbelts indicates the occurrence of highly-ordered self-assembly. In contrast, complex **Pt-2** is found to assemble into well-defined nanospheres and microcubes in non-polar solvents. (3) The hydrophobic chiral camphorone groups not only increase the colloidal stability of the aggregates but also help to modulate the configuration of molecular packing *via* the large steric hindrance. Through changing the linker of the chiral camphorone motif, the transfer of chirality and regioisomerism can be effectively adjusted, which influences their self-assembly capability and resultant nanostructures in mixed solvents. As a result, remarkable amplification of circular dichroism (CD) and CPL signals from small molecules to nanotwists was observed for both pairs of complexes **Pt-1** and **Pt-2**. For comparison, two enantiomeric pairs of neutral Pt(II) complexes **Pt-3–Pt-4** with similar structures have been synthesized and investigated.

## Results and discussion

### Synthesis and characterization

The synthetic routes of the desired ligands **L1–L4** and complexes **Pt-1–Pt-4** are illustrated in Schemes S1 and S2, and the detailed procedures and characterization data are given in the ESI.† The cationic Pt(II) complexes **Pt-1–Pt-2** and neutral complexes **Pt-3–Pt-4** were prepared in moderate to high yields by the reaction of the chloroplatinum(II) precursor with the corresponding chiral isocyanide ligands or the chiral acetylene ligands, respectively. All new ligands and complexes were fully confirmed by $^{1}$H NMR, $^{13}$C NMR, and high-resolution mass spectroscopy (HRMS) as well as Fourier transform infrared (FT-IR), as shown in Fig. S1–S25 (ESI†). Intense absorption bands of $\nu$(N≡C) were observed at higher frequency (*ca.* 2185 and 2188 cm$^{-1}$) for complexes **Pt-1** and **Pt-2**, comparing to the corresponding acetylene ligands based **Pt-3** and **Pt-4** at *ca.* 2100 and 2098 cm$^{-1}$ for the absorption bands of $\nu$(C≡C), respectively, further confirming the successful synthesis of the complexes (Fig. S25, ESI†).

### X-Ray crystallography

The successful synthesis of ligands was also confirmed by single-crystal X-ray analyses. Suitable single crystals of ligands **L2–L4** were obtained by slow evaporation in ethyl acetate solutions and their crystal structures were determined. The molecular structures of ligands **L2–L4** are shown in Fig. S26–S28 (ESI†), and the crystal structure determination data are summarized in Table S1 (ESI†). D-**L2** crystallizes in the triclinic $P\bar{1}$ space group, while L-**L3** and L-**L4** crystallize in the orthorhombic $P212121$ space groups (Table S1, ESI†). Crystal structural analysis of ligand **L2** revealed that the unit cell contained two independent molecules with distinct conformations (referred to as **L2a** and **L2b**, see Fig. S26a, ESI†). For the ligands **L2** and **L4**, the benzene ring is nearly perpendicular to the sulfonamide plane with dihedral angles of 80.48° (**L2a**), 73.65° (**L2b**), and 78.6° (**L4**), indicating the presence of dihedral angles intramolecular N–H···O=C hydrogen bonding, together with intramolecular N–H···O=C hydrogen bonding (Fig. S27, ESI†). Ligand **L2a** displays a C=O···H–N distance of 2.915 Å, which is quite similar to that of ligand **L4** with 2.886 Å. Because of loose intramolecular seven-membered rings hydrogen bonding, the formation of intermolecular hydrogen bonds can be assumed for ligands **L2** and **L4** (2.232 Å and 2.213 Å for ligand **L2**, 2.250 Å for ligand **L4**, Fig. S28, ESI†). Interestingly, the amide torsion angle and dihedral angle between the amide plane and the benzene ring groups of ligand **L3** are 4.51° and 4.37°, respectively, which is almost planar in the crystal. Ligand **L3** displays a C=O···H–N distance of 1.970 Å and a C=O···H distance of 2.275 Å, in the formation of two fused six-member rings. Unfortunately, intensive efforts to grow single crystals for all these complexes were unsuccessful. Thus, the geometries of **Pt-1** and **Pt-2** were optimized in $CH_3CN$ using density functional theory (DFT) (Fig. S29, ESI†). In stark contrast to **Pt-2**, the optimized geometry of complex **Pt-1** displayed that the benzene ring, amide group, and carbonyl group on the camphorone motif are almost coplanar, which is consistent with the single crystal structure of **L3**.

### Spectroscopic studies in solution

Before studying the self-assembly behaviors, the photophysical properties of **Pt-1–Pt-4** were investigated systematically in solution (Fig. 1 and Fig. S30–S33, ESI†). The simulated UV-vis absorption spectra *via* TDDFT calculation and the comparison to those of the experimental spectra are provided in Fig. S34 (ESI†). The theoretical spectra could reproduce the experimental spectra features very well.

As shown in Fig. 1a, the absorption spectra of complexes **Pt-1–Pt-2** in dilute chloroform ($10^{-5}$ M) possessed moderate intense absorption bands below *ca.* 340 nm, and weak absorption bands between 390 and 450 nm. Based on the molar extinction coefficients, the calculated natural transition orbitals (NTO, Tables S2 and S3, ESI†), we attributed the high-energy absorption bands to the intra-ligand ($^{1}$IL) $^{1}\pi$–$\pi^{*}$ transitions of the C^N^N ligand and the low-energy absorption bands to $^{1}$MLCT/$^{1}$LLCT of the C^N^N ligand transitions.[34]

The absorption spectra of **Pt-3–Pt-4** in $CHCl_3$ solution show high-energy absorption bands in the range of 290–400 nm, and broad low-energy absorption bands between *ca.* 410 and 500 nm. The former can be attributed to intraligand charge-transfer ($^{1}$ILCT) transitions of the (C^N^N) ligand, while the latter can be assigned mainly to $^{1}$MLCT transitions.[35] This character of transition was further confirmed by NTOs (Tables S2 and S3, ESI†).

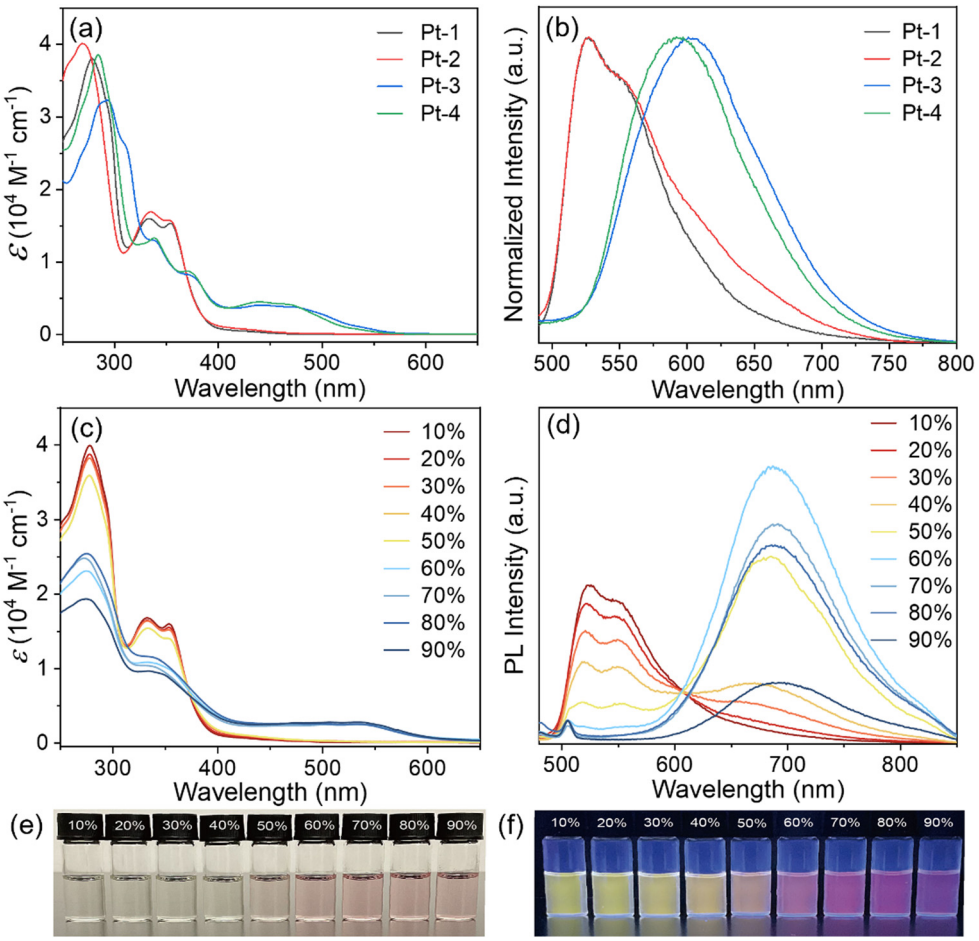


Fig. 1 (a) UV-Vis absorption and (b) normalized PL spectra excited at 420 nm of complexes **Pt-1**, **Pt-2**, **Pt-3**, and **Pt-4** in dilute $CHCl_3$; (c) UV-Vis and (d) emission spectra of **Pt-1** in $CHCl_3$-MCH with different MCH fractions (vol, 10–90%); and photographs of complex **Pt-1** in the $CHCl_3$-MCH mixture excited at 420 nm under visible light (e) and 365 nm UV light (f) irradiation.

Complexes **Pt-1** and **Pt-2** are soluble in $CHCl_3$, THF, and $CH_3CN$, whereas their solubility in nonpolar solvents such as hexane and methylcyclohexane (MCH) is very poor. Thus, the self-assembly behaviors of these complexes were examined in the mixed solvents of $CHCl_3$ and MCH with different ratios. For complex **Pt-1**, when the MCH content in $CHCl_3$ reaches *ca.* 40%, the slightly reduced absorption band intensity indicates the formation of well-dispersed nanoaggregates of **Pt-1**$_{agg-I}$. Upon the increase of MCH content to *ca.* 60%, complex **Pt-1** showed a dramatic high-energy absorbance decrease, along with the emergence of a new absorption shoulder at *ca.* 400–600 nm. On the basis of the other related studies,[15,36] the newly formed absorption band should be originating from the metal–metal-to-ligand charge transfer ($^1$MMLCT) transition, indicating the formation of new aggregate species, namely **Pt-1**$_{agg-II}$. Thus, it is very promising to construct controllable nanoscale structures with various morphologies for complex **Pt-1**. Similarly, upon increasing the MCH content in chloroform solutions for **Pt-2** (Fig. S35, ESI†), an additional absorption band appears at *ca.* 566 nm, which is also assigned as the $^1$MMLCT band. However, the growth of an apparent new absorption band was not observed in the cases of **Pt-3** and **Pt-4** (Fig. S36 and S37, ESI†).

The emission spectra on the solvent effect of complexes **Pt-1**–**Pt-4** in $CHCl_3$/MCH mixtures were also recorded (Fig. 1d and Fig. S35–S37, ESI†). Complex **Pt-1** in $CHCl_3$ exhibited an emission maximum at *ca.* 528 nm with a quantum yield of 4.0% and a lifetime ($\tau$) of 537 ns (Table S4, ESI†). It is anticipated that the presence of transition metal Pt atoms possessed large spin–orbit coupling constants that can assist in facile intersystem crossing from single excited states to triplet excited states.[15] Considering the large Stokes shifts, relatively long lifetimes, and TDDFT calculations, we assigned the emission band for **Pt-1** to the triplet excited state $^3$MLCT/$^3$LLCT character.[34] The relatively low emission efficiency may partially be caused by the quenching of molecular oxygen in the solution. Upon increasing the MCH content in the $CHCl_3$/MCH mixture, the emission band at 525 nm decreased gradually, along with the appearance of a new emission band at around 687 nm with a quantum yield of 9.0% and lifetime ($\tau$) of 229 ns, which can be ascribed to $^3$MMLCT character.[15,36] A similar phenomenon has been observed for complex **Pt-2** (Fig. S35, ESI†). On the contrary, the emission-quenching phenomena of **Pt-3** and **Pt-4** in nonpolar solvents were observed (Fig. S36-S37, ESI†). Such emission enhancement in high MCH content for complex **Pt-1** could

 

be attributed to the formation of aggregates **Pt-1**$_{agg\text{-}II}$ induced by solvophobic interactions and Pt···Pt/π–π interactions with the increasing of non-polar solvent.

### CD and CPL properties of self-assemblies

To further clarify the chirality transfer and amplification, the circular dichroism (CD) and CPL spectra of complexes **Pt-1–Pt-4** were carried out (Fig. 2 and Fig. S38–S41, ESI†). As shown in Fig. 2a, a pair of weak mirror-image CD spectra of complexes **D/L-Pt-1** appeared at *ca.* 300 nm in the diluted chloroform solution (50 μM). The weak Cotton effect at the band of 300 nm revealed that the chirality was transmitted from the camphorone group to the originally achiral pincer C^N^N ligand. Remarkably, a bisignated CD signal with a positive Cotton effect at 283 nm and a negative Cotton effect at 395 nm was observed for **D-Pt-1** in the solution of $CHCl_3$/MCH (2/8, v/v, 50 μM), with a $CD_{max}$ amplified by *ca.* 70-fold. A similar mirror-image CD spectrum was obtained for **L-Pt-1** assemblies, indicating the induction of chirality with opposite handedness from enantiomers. Surprisingly, a $CD_{max}$ amplified by *ca.* 150-fold was found for **Pt-2** in the solution of $CHCl_3$/MCH (2/8, v/v, 50 μM) compared to the monomeric species. More intriguingly, both **Pt-1** and **Pt-2** assemblies showed intense bisignated CPL signals with relatively high $|g_{lum}|$ values of 0.013 and 0.023, which may benefit from the effective exciton coupling of assemblies at excited states. These observations suggest that the chirality for complexes **Pt-1** and **Pt-2** is not only transferred from the molecules into the supramolecular polymers but also significantly amplified due to the strong intermolecular π–π interaction and hydrogen bonds. Furthermore, the chirality is amplified from the molecular level to the higher-ordered chiral assemblies through π–π and strong intermolecular hydrogen bond interactions. In sharp contrast, no prominent chirality amplification for complexes **Pt-3** and **Pt-4** was observed during the supramolecular polymerization process (Fig. S40 and S41, ESI†). Such dramatic spectroscopic behaviors for cationic and neutral complexes may be attributed to their solubility difference in nonpolar solvents and hence assembly performance variations, suggesting the importance of the solvophobic interactions in the self-assembly process.

### Morphology studies of self-assemblies

To gain deep insight into the self-assembly behaviors of **Pt-1–Pt-4**, scanning electron microscopy (SEM), transmission electron microscopy (TEM), the aberration-corrected high-angle annular dark-field scanning TEM (HAADF-STEM), and atomic force microscopy (AFM) were further employed for morphology studies. Delightedly, well-defined morphologies for complex **Pt-1**, including nanotwists, nanorings, dendritic twists, and nanorods were formed (Fig. 3, and Fig. S42–S46, ESI†) through the screening of simple parameters, *i.e.*, temperatures, mixed solvent ratios, and concentrations. In general, when 80% MCH was added to the $CHCl_3$ solution of complex **Pt-1**, the morphologies of uniform short fibers with lengths of a few hundred nanometers were observed (Fig. S42, ESI†). With the MCH content decreasing to 60%, these molecules formed longer nanofibers with an average *ca.* 40 nm in width and tended to form bent twisted nanostructures. More interestingly, the SEM images of **Pt-1** in 40% MCH in $CHCl_3$ solution showed unique toroidal nanostructures with an average of external diameters

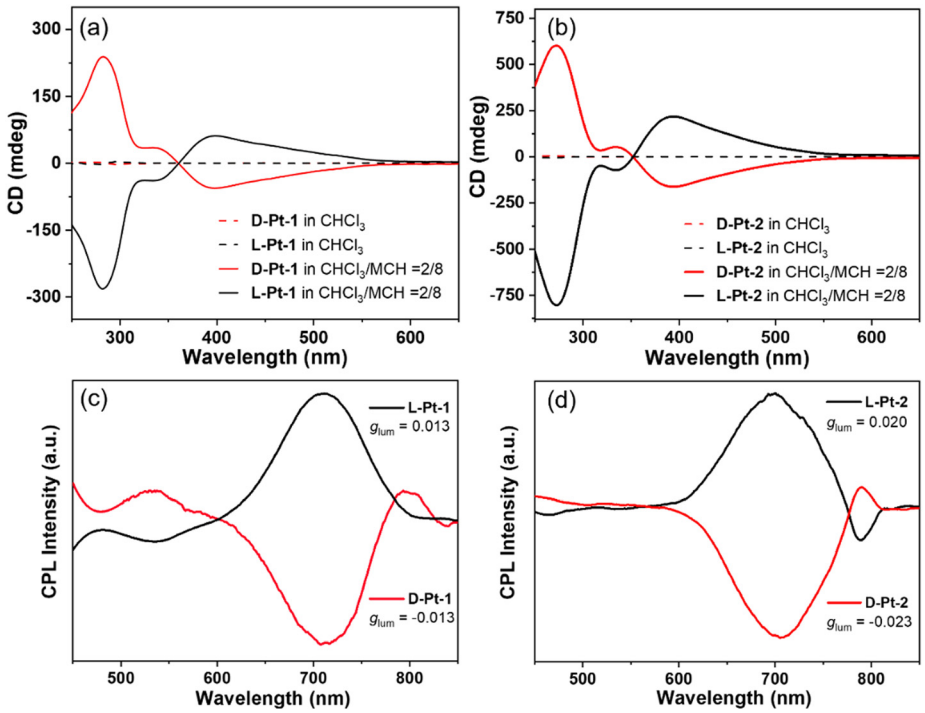


Fig. 2 CD spectra of complexes **D/L-Pt-1** (a) and **D/L-Pt-2** (b) in $CHCl_3$ and in the MCH-$CHCl_3$ mixture (2/8, v/v); CPL spectra excited at 420 nm of complexes **D/L-Pt-1** (c) and **D/L-Pt-2** (d) in the MCH-$CHCl_3$ mixture (2/8, v/v) ($c$ = 50 μM).

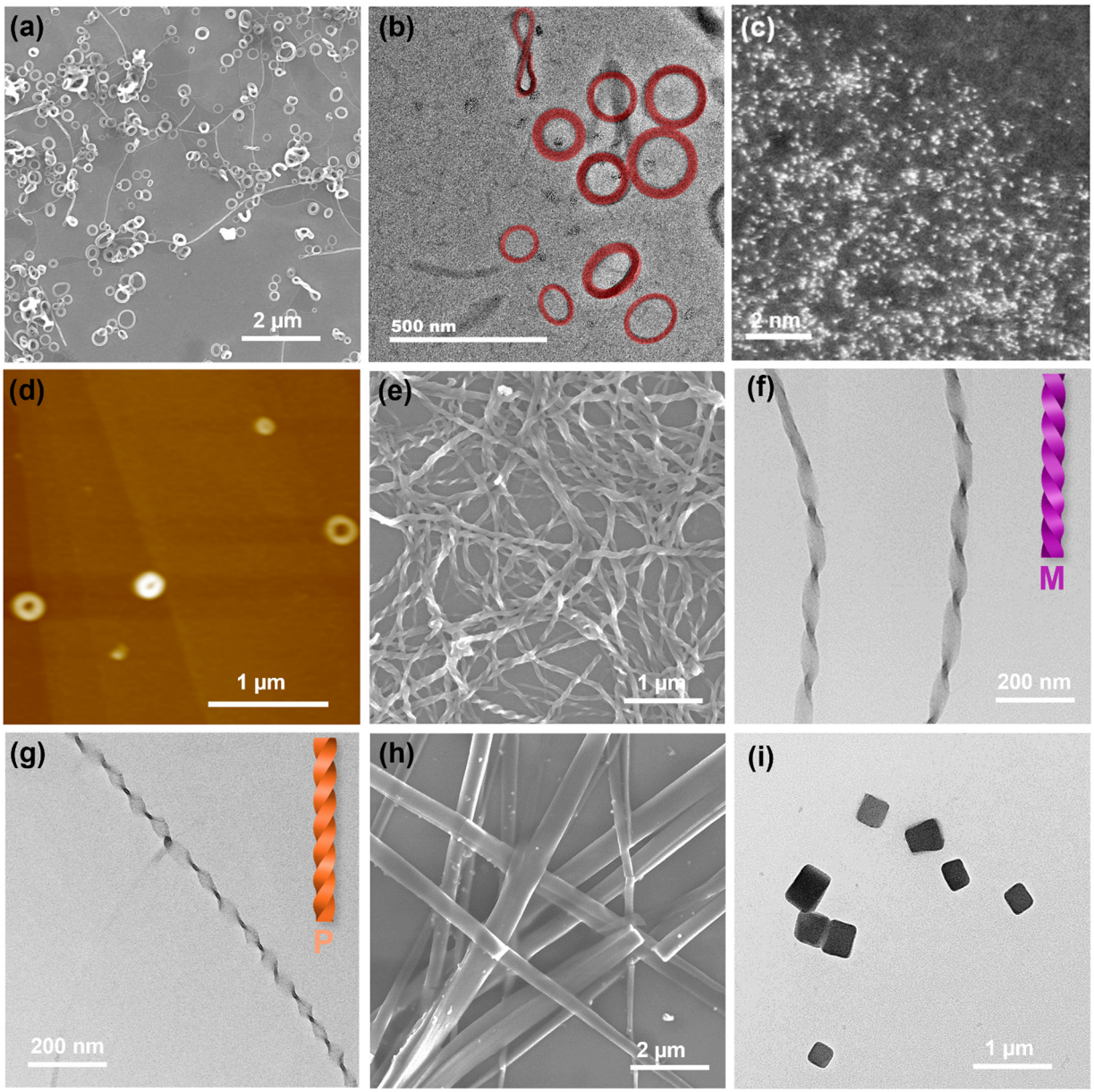


Fig. 3 (a–d) SEM, TEM, HAADF-STEM and AFM images of **D-Pt-1** self-assemblies prepared in 40% MCH-$CHCl_3$ solution at R.T. without aging (the nanorings highlighted as red); (e and f) SEM and TEM images of **D-Pt-1** self-assemblies prepared in 40% MCH-$CHCl_3$ solution after aging for 2 h at 288 K; (g) TEM image of **L-Pt-1** self-assemblies prepared in 40% MCH-$CHCl_3$ solution after aging for 2 h at 288 K; (h) SEM image of **D-Pt-1** self-assemblies prepared in 40% MCH-$CHCl_3$ solution after aging for 3 days; (i) TEM images of **D-Pt-2** self-assemblies prepared in 40% MCH-$CHCl_3$ solution after aging for 16 h at R.T.

*ca.* 230 nm (Fig. 3a). Smaller toroidal nanostructures were further confirmed from TEM, HAADF-STEM, and AFM images (Fig. 3b–d and Fig. S43, S44, ESI†), which indicated the height of the nanorings to be *ca.* 8 nm (Fig. S44, ESI†). The HAADF-STEM images and corresponding EDS mapping analyses (Fig. 3c and Fig. S44, S45, ESI†) not only confirmed the self-assemblies but also provided evidence for Pt···Pt interactions by measuring the distance between the neighboring Pt atoms.[37] The ring closure of the supramolecular polymers requires both the bending and cyclization processes of twisted fibers, which can be facilitated by kinetic control of gentle sonication.

When cooling the temperature to 288 K, essentially long nanotwists with an average width of about 90 nm were observed for both complexes **D-Pt-1** and **L-Pt-1** (Fig. 3e and Fig. S45, ESI†). The supramolecular chirality of the assemblies was also observed using SEM. Interestingly, left-handed (M) twists appeared from the solution of complex **D-Pt-1** while the opposite right-handed (P) twists were formed using the L-enantiomer, which is consistent with the results from the CD spectra studies mentioned above. With the prolongation of the self-assembly time to 12 h, the initially formed uniform twist nanostructures subsequently entangled with others to grow into higher-order dendritic twist

 

structures (Fig. S46a–c, ESI†). After 3 days, precipitates were dominated by microbelt structures with lengths of a few hundred micrometers as revealed in the corresponding SEM images (Fig. 3h and Fig. S46f, ESI†). This indicated that upon aging the $CHCl_3$-MCH (60/40, v/v, 50 μM) of complex **Pt-1** at 288 K, the initially assembled nanofibers grew gradually into the twists, dendritic twists, and finally microbelts. Overall, we found that the nanotwists or nanoring structures were formed in hours, while the microbelts were generated after days of aging.

In sharp contrast, complex **Pt-2** linked with the sulfamide group showed different aggregated species under similar conditions. Nanospheres with diameters of *ca.* 100 nm have been observed in a $CHCl_3$-MCH (60/40, v/v, 50 μM) mixture (Fig. S47, ESI†). Prolonged standing time results in forming cubic nanostructures (Fig. 3i and Fig. S48, ESI†), which can be promoted by reducing the content of MCH to 20% (Fig. S47, ESI†). Such differences in the self-assembly behaviour and morphologies of complex **Pt-2** can be attributed to a different packing conformation caused by the slight structural modification, suggesting the significance of the "kinetically trapped" design in **Pt-1**. Whereas for **Pt-3** and **Pt-4**, only monodispersed nanospheres were observed (Fig. S49 and S50, ESI†).

### Structural elucidation of the assemblies

To further understand the self-assembly process, variable-temperature UV-vis absorption was performed in the mixed solvent of 1,1,2,2-tetrachloroethane (TCE), and MCH (3 : 7, v/v, TCE was employed as a higher boiling point than $CHCl_3$) at a concentration of 20 μM. As shown in Fig. 4a, upon slow heating (1 K $min^{-1}$) of the mixture of **Pt-1$_{agg-II}$** from 298 K to 363 K, the absorption bands at *ca.* 280 nm and 335 nm gradually increased, along with the disappearance of the shoulder at *ca.* 540 nm. The UV-vis profile of complex **Pt-1** at 363 K is very similar to that in pure $CHCl_3$, suggesting predominant molecular monomeric species at high temperatures, indicating the depolymerization of aggregates **Pt-1$_{agg-II}$** of complex **Pt-1** (Fig. 4a). By plotting the degree of aggregation ($\alpha_{agg}$)[38] against temperature from UV-vis absorption at 290 nm, a non-sigmoidal heating curve with a very high elongation temperature (*ca.* 358 K) can be obtained, which evidenced that the formation of **Pt-1$_{agg-II}$** proceeds *via* a cooperative nucleation-elongation mechanism.[38–40] The negative enthalpy polymerization process (Table S5, ESI†) is consistent with aggregation arising from the involvement of intermolecular Pt···Pt/π–π interactions and multiple hydrogen bonds as discussed above. Nevertheless, the current variable-temperature data fitting model is not suitable for understanding the complex assembly process of this complex quite well. To better understand the assembly process of this complex, a more detailed variable-temperature data fitting model is needed. However, **Pt-1$_{agg-II}$** will transform into more thermodynamically stable micro-belt aggregates at high temperatures.

In order to gain insights into the interaction patterns dictating during the supramolecular polymerization, concentration-dependent and temperature-dependent $^1$H NMR experiments of **Pt-1–Pt-4** were carried out (Fig. 4b and Fig. S51–S55, ESI†). Increasing the concentration results in pronounced upfield shifts for the protons of complex **Pt-1** in the aromatic region, indicative of the strong shielding effect induced by the formation of aggregates through intermolecular π–π/Pt···Pt interactions. Simultaneously, only slight shifts for the amide N–H proton were observed from 9.53–9.49 ppm. Meanwhile, the variable-temperature $^1$H NMR spectra of **Pt-1** in $CD_3CN$ showed a very similar phenomenon upon cooling the temperature from 343 K to 283 K (Fig. S51, ESI†). A plausible explanation would be the formation of the closed-form monomeric species caused by the highly stable intramolecular hydrogen bonding between the amide N–H group and the camphorone carbonyl group (Scheme 1). Notably, the open-form monomeric species was not visible even at high temperatures, most likely

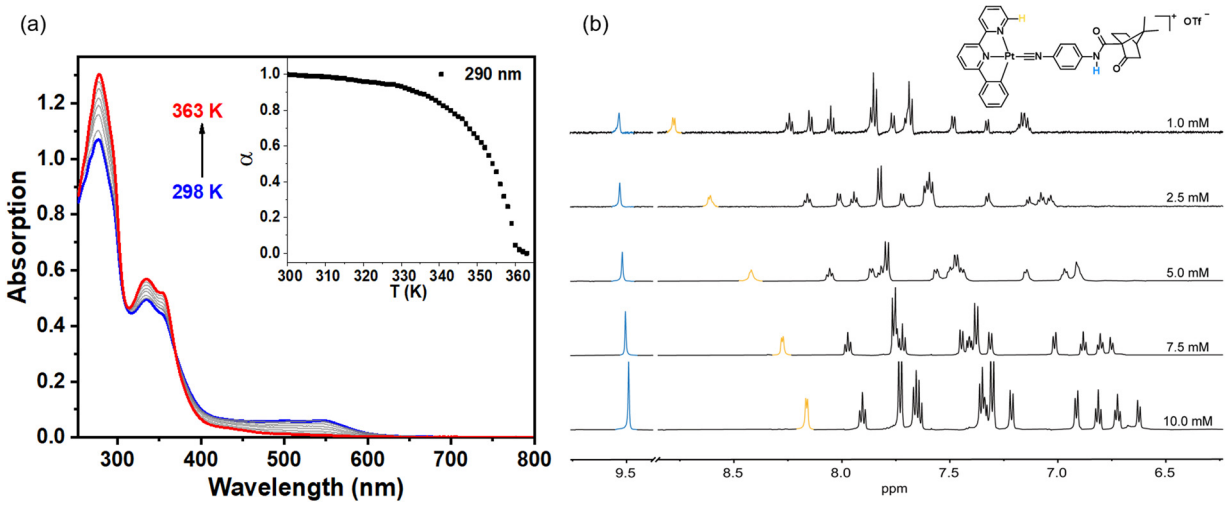


Fig. 4 (a) Temperature-dependent UV-Vis absorption spectra of complex **Pt-1** in a mixture of TCE/MCH (v/v, 3/7, $c$ = 50 μM) upon heating from 298 K (red line) to 363 K (blue line) with a rate of 1 K $min^{-1}$ showing from the transformation from **Pt-1$_{agg-II}$** to **Pt-1$_{mono}$**. Inset: Degree of **Pt-1$_{agg-II}$** ($\alpha_{agg}$) monitored at 290 nm *vs.* temperature. (b) Concentration-dependent $^1$H NMR spectra of **Pt-1** in $CD_3CN$ at 298 K.

due to the very strong strength of intramolecular hydrogen bonding, which is consistent with the formation of two fused six-membered rings as mentioned above.

Upon increasing the concentration for **Pt-2**, the aromatic proton signals also undergo apparent up-field shifts, whereas the amide N–H signal was found to down-field shift (Fig. S52, ESI†). A similar phenomenon was observed for complex **Pt-2** in the temperature-dependent $^{1}$H NMR experiments (Fig. S53, ESI†). These observations indicate the formation of intermolecular hydrogen bonds from the monomeric species for **Pt-2**. On the basis of the concentration-dependent $^{1}$H NMR spectra, **Pt-3** and **Pt-4** were found to exhibit similar variation tendency but much fewer changes than those of **Pt-1** and **Pt-2**, indicating negligible intermolecular π–π/Pt···Pt interactions for **Pt-3** and **Pt-4**. It is worth noting that the protons ascribable to camphorone rings experience almost no shift for all these complexes, which indicates no aggregation formation for camphorone rings. Taking all the above spectroscopic evidence into account, it is possible to shed some light on the aggregation mode of all these complexes, particularly the potential role of the linker units to participate in competing intra- *vs.* intermolecular hydrogen bonding and π–π/Pt···Pt interactions during the process of self-assembly. Among them, we infer that the equilibrium between intramolecular hydrogen bonding (closed conformation) and non-hydrogen bonding states (extended conformation) of complex **Pt-1** affords the expected kinetically trapped assembling system.

### Proposed self-assembly pathway

On the basis of the photophysical data, electronic microscopic studies as well as NMR data, a proposed polymorphic assembly pathway for **Pt-1** is suggested as depicted in Fig. 5. The chiral camphorone moieties are considered to have higher solubility towards non-polar solvent, whereas the platinum cores tightly pack in the inner core of the assembly. Upon adding a small fraction of MCH (20–40%) to the $CHCl_3$ solution of **Pt-1**, the positively charged tridentate cyclometalated platinum(II) isocyanide moiety became less solvated, indicating that the solvophobic interactions serve as the predominant driving force that would bring the Pt(II) moieties into close proximity for the formation of weak π–π/Pt···Pt interactions. Furthermore, the supramolecular Pt···Pt chains are perturbed by the electrostatic repulsion between two neighboring Pt(II) cations, which subsequently induces the distortion and undergoes self-assembly into toroidal nanostructures **Pt-1**$_{\mathbf{agg\text{-}I}}$, appended with the "close-form" amide substituted camphorone as the exterior. In such mixture compositions, no MMLCT band can be observed in the UV-vis spectra, although new $^{3}$MMLCT emission bands can

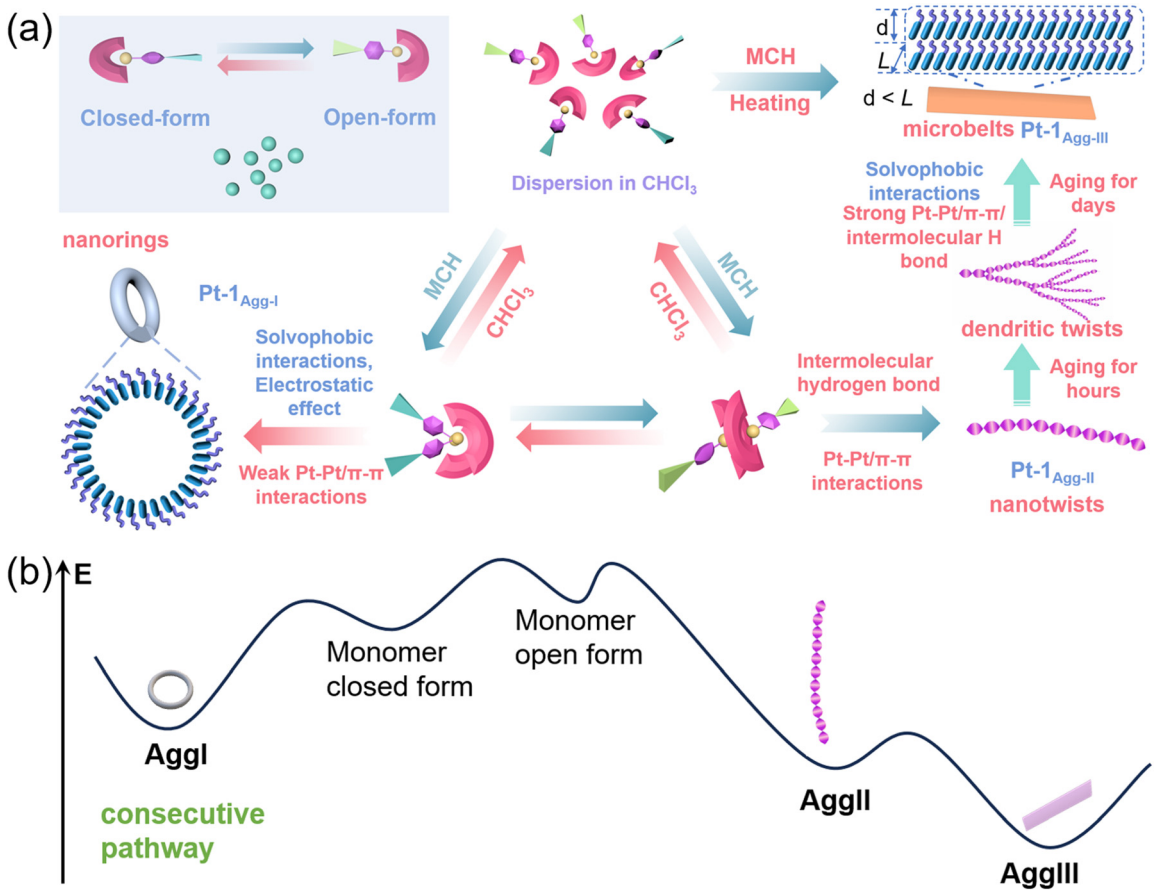


Fig. 5 (a) Cartoon representation of the supramolecular polymerization pathways for **Pt-1**. (b) The energy landscape of the consecutive supramolecular polymerization for **Pt-1**.

 

be observed upon increasing the MCH content, indicating the formation of well-dispersed oligomers in the solution. With the increasing MCH content to *ca.* 60%, complex **Pt-1** tends to form nanotwist structures **Pt-1$_{agg\text{-}II}$** with Pt···Pt/π–π and intermolecular hydrogen bonding interactions induced by stronger solvophobic interactions, evidenced from the MMLCT absorption shoulders, the $^{3}$MMLCT emission bands, and the HAADF-STEM images. Upon hours of aging, the nanotwists tended to grow into higher-order structures (Fig. S46, ESI†), *i.e.*, dendritic twists. With prolonged aging time to days, such formation of solvophobic interactions together with strong intermolecular hydrogen bonding and π–π/Pt···Pt interactions would restrict the assemblies in alignment, resulting in linear growth and formation of thermodynamically stable microbelts with orderly and tightly arrangement finally (Fig. 5), which is further confirmed by the PXRD data (Fig. S56, ESI†). Due to the energy barrier for the formation, the transformation from nanotwists **Pt-1$_{agg\text{-}II}$** to microbelts **Pt-1$_{agg\text{-}III}$** is relatively slow without any perturbation (several days). However, this transformation can be facilitated by heating the **Pt-1$_{agg\text{-}II}$** solution to 313 K, thus, the appearance of microbelts is significantly shortened. The reason can be rationalized that heating the solution could accelerate the transformation of intramolecular hydrogen bonds to intermolecular ones, which provides additional driving forces for molecular self-assembly. Once the nuclei are formed, they can act as seeds to promote the transformation of metastable **Pt-1$_{agg\text{-}II}$** into thermodynamically stable **Pt-1$_{agg\text{-}III}$**.

On the other side, molecules of complex **Pt-2** would assemble into nanospheres with the transition metal center Pt part as the core while loosely packing camphorone motif as a shell, due to the steric hindrance of the bridgehead methyl moiety in methylene sulfonamide substituted camphorone. With the alignment of the metallophilic interactions, the complex would gradually transform from nanospheres into nanocubes upon the prolongation of standing time.

The distinct mechanisms during the self-assembly of amide-bearing **Pt-1** and ester-bearing **Pt-2** should probably lie in the modulation of the hydrogen bonding interaction, which leads to different organizations of the complex. Moreover, the formation of two six-member rings *via* intramolecular hydrogen bonds in complex **Pt-1** increased the rigidity of the isocyanide ligand, accordingly resulting in closer packing. Whereas **Pt-3** and **Pt-4** are less tightly assembled into nanospheres to reduce the surface energy.

## Conclusions

In summary, four pairs of chiral camphorone-functionalized enantiomeric platinum complexes **D/L-Pt-1–Pt-4** are reported, and they have shown the ability to form a variety of distinct morphologies. Such a self-assembly process is governed by the Pt···Pt/π–π stacking and the solvophobic interactions as well as electrostatic repulsion provided by the positively charged tridentate cyclometalated platinum(II) moieties. The polymorphic self-assembly with well-defined nanostructures, *i.e.* nanorings, nanotwists, dendritic twists, and microbelts in various conditions, accompanied by dramatic spectroscopic changes, were systematically investigated by photophysical studies, and electron microscopy. Two pairs of enantiomers **D/L-Pt-1–Pt-2** showed significantly amplified effects for chirality and circularly polarized luminescence in their corresponding nanoassemblies. The current work demonstrates that the incorporation of chiral auxiliary ligands into Pt(II) complexes would make them desirable for the creation of various functional supramolecular materials with outstanding chirality and circularly polarized luminescent properties.

## Experimental section

All chemical reagents were purchased from commercial sources (Aldrich, Alfa Aesar, Energy Chemical, and Adamas) and were used as received unless otherwise noted. $^{1}$H NMR and $^{13}$C NMR spectra were recorded on a 600 MHz BRUKER spectrometer at room temperature using tetramethylsilane (TMS) as the internal standard. High-resolution mass spectrometry (HRMS) data were collected on a Bruker maxis UHR-TOF mass spectrometer in the ESI-positive mode. Fourier transform infrared (FT-IR) measurements were performed using a Bruker Tensor27 spectrophotometer. Powder X-ray diffraction (PXRD) patterns were recorded on a Bruker D8 Advance instrument. X-ray single crystal diffraction data were collected on a Nonius Kappa CCD diffractometer using Mo Kα radiation (λ) 0.71073 Å (graphite monochromator). UV-vis spectra were recorded on an Agilent Technologies Cary 3500 spectrometer. Emission spectra and the absolute quantum yields were recorded on a Horiba FluoroMax Plus spectrofluorometer. CD experiments were performed using a Chirascan CD spectrometer. PL lifetimes were measured using an FLS1000 fluorescence spectrometer (Edinburgh) at room temperature. CPL spectra and subsequently derived glum values were recorded using an OLIS CPL Solo spectrofluorometer and the globalworks software suite. Scanning electron microscopy (SEM) was performed using a Hitachi SU8220 instrument. Transmission electron microscopy (TEM) was performed using a Hitachi TEM HT 7800 instrument operating at 80 kV acceleration voltage. The high-angle annular dark-field (HAADF) imaging and EDX images were obtained using an FEI Titan cubed Themis G2 300 microscope operated at 300 kV and equipped with a probe aberration corrector and a monochromator. The samples were dropped onto a carbon-coated copper grid and dried. Atomic force microscopy (AFM) experiments were performed on an Asylum Research Cypher VRS (Oxford instruments) atomic force microscope equipped with a Scan Asyst-HR fast scanning module and a Scan Asyst Air-HR probe (tip radius, 2 nm), utilizing peak force feedback control. Density functional theory (DFT) and TDDFT calculations of these complexes were performed using Gaussian 09 software using the B3LYP, and the LANL2DZ basis set was assigned for the Pt atom and 6-31G* basis set for all the remaining atoms. Multiwfn software was used for NTO analyses.[41] Detailed synthesis and experimental procedures are described in the ESI.†

## Author contributions

X. Zhu: investigation, conceptualization, data curation, methodology, visualization, writing – original draft, review, and editing, funding acquisition. Z. Wang: investigation, visualization, writing – original draft. Y. Jia: investigation. F. Yang: methodology. Y. Zhang: methodology. Shirui Zhao: investigation. X. He: supervision, conceptualization, funding acquisition.

## Conflicts of interest

There are no conflicts to declare.

## Acknowledgements

This study was supported by the National Natural Science Foundation of China (22202128), Fundamental Research Funds for the Central Universities (GK202205016, GK202201006, and 2021CSLY010), China Postdoctoral Science Foundation (No. 2020M683417), and the Natural Science Basic Research Plan in Shaanxi Province of China (2021JQ-302).



## Notes and references

1 S. S. Babu, V. K. Praveen and A. Ajayaghosh, *Chem. Rev.*, 2014, **114**, 1973–2129.
2 F. Wurthner, *Acc. Chem. Res.*, 2016, **49**, 868–876.
3 J. D. Tovar, *Acc. Chem. Res.*, 2013, **46**, 1527–1537.
4 D. B. Amabilino, D. K. Smith and J. W. Steed, *Chem. Soc. Rev.*, 2017, **46**, 2404–2420.
5 J. Li, J. Wang, H. Li, N. Song, D. Wang and B. Z. Tang, *Chem. Soc. Rev.*, 2020, **49**, 1144–1172.
6 L. Zhang, H. X. Wang, S. Li and M. Liu, *Chem. Soc. Rev.*, 2020, **49**, 9095–9120.
7 S. Yagai, Y. Kitamoto, S. Datta and B. Adhikari, *Acc. Chem. Res.*, 2019, **52**, 1325–1335.
8 P. K. Hashim, J. Bergueiro, E. W. Meijer and T. Aida, *Prog. Polym. Sci.*, 2020, **105**, 101250.
9 P. A. Korevaar, S. J. George, A. J. Markvoort, M. M. Smulders, P. A. Hilbers, A. P. Schenning, T. F. De Greef and E. W. Meijer, *Nature*, 2012, **481**, 492–496.
10 A. Sorrenti, J. Leira-Iglesias, A. J. Markvoort, T. F. A. de Greef and T. M. Hermans, *Chem. Soc. Rev.*, 2017, **46**, 5476–5490.
11 C. Fouquey, J.-M. Lehn and A.-M. Levelut, *Adv. Mater.*, 1990, **2**, 254–257.
12 S. W. Englander and L. Mayne, *Proc. Natl. Acad. Sci. U. S. A.*, 2014, **111**, 15873–15880.
13 Y. Tezuka, *Acc. Chem. Res.*, 2017, **50**, 2661–2672.
14 N. Baumer, J. Matern and G. Fernandez, *Chem. Sci.*, 2021, **12**, 12248–12265.
15 V. W. Yam, V. K. Au and S. Y. Leung, *Chem. Rev.*, 2015, **115**, 7589–7728.
16 M. C. Yeung and V. W. Yam, *Chem. Soc. Rev.*, 2015, **44**, 4192–4202.
17 Z. Gao, Y. Han, Z. Gao and F. Wang, *Acc. Chem. Res.*, 2018, **51**, 2719–2729.
18 A. Aliprandi, D. Genovese, M. Mauro and L. De Cola, *Chem. Lett.*, 2015, **44**, 1152–1169.
19 Y. Chi and P. T. Chou, *Chem. Soc. Rev.*, 2010, **39**, 638–655.
20 J. Herberger and R. F. Winter, *Coord. Chem. Rev.*, 2019, **400**, 213048.
21 R. Chakrabarty, P. S. Mukherjee and P. J. Stang, *Chem. Rev.*, 2011, **111**, 6810–6918.
22 V. W.-W. Yam, A. K.-W. Chan and E. Y.-H. Hong, *Nat. Rev. Chem.*, 2020, **4**, 528–541.
23 M. Wehner and F. Würthner, *Nat. Rev. Chem.*, 2019, **4**, 38–53.
24 J. Matern, Y. Dorca, L. Sanchez and G. Fernandez, *Angew. Chem., Int. Ed.*, 2019, **58**, 16730–16740.
25 X. Wang, G. Guerin, H. Wang, Y. Wang, I. Manners and M. A. Winnik, *Science*, 2007, **317**, 644–647.
26 J. S. Valera, R. Gomez and L. Sanchez, *Angew. Chem., Int. Ed.*, 2019, **58**, 510–514.
27 H. Chen, Z. Huang, H. Wu, J. F. Xu and X. Zhang, *Angew. Chem., Int. Ed.*, 2017, **56**, 16575–16578.
28 T. E. Kaiser, H. Wang, V. Stepanenko and F. Wurthner, *Angew. Chem., Int. Ed.*, 2007, **46**, 5541–5544.
29 M. J. Mayoral, C. Rest, V. Stepanenko, J. Schellheimer, R. Q. Albuquerque and G. Fernandez, *J. Am. Chem. Soc.*, 2013, **135**, 2148–2151.
30 A. Langenstroer, K. K. Kartha, Y. Dorca, J. Droste, V. Stepanenko, R. Q. Albuquerque, M. R. Hansen, L. Sanchez and G. Fernandez, *J. Am. Chem. Soc.*, 2019, **141**, 5192–5200.
31 J. Matern, K. K. Kartha, L. Sanchez and G. Fernandez, *Chem. Sci.*, 2020, **11**, 6780–6788.
32 Y. Zhang, N. Zhou, X. Zhu and X. He, *Polym. Chem.*, 2021, **12**, 5535–5541.
33 L. Li, N. Zhou, H. Kong and X. He, *Polym. Chem.*, 2019, **10**, 5465–5472.
34 S.-W. Lai, H.-W. Lam, W. Lu, K.-K. Cheung and C.-M. Che, *Organometallics*, 2002, **21**, 226–234.
35 W. Liu, B.-X. Mi, M. C. W. Chan, Z. Hui, C.-M. Che, N. Zhu and S.-T. Lee, *J. Am. Chem. Soc.*, 2004, **126**, 4958–4971.
36 K. M.-C. Wong and V. W.-W. Yam, *Acc. Chem. Res.*, 2011, **44**, 424–434.
37 HAADF-STEM images provide direct and valuable information such as atomic distance, and relative height differences between adjacent Pt atoms according to the different brightness of various atoms. For more information, see ref: J. Shan, C. Ye, Y. Jiang, M. Jaroniec, Y. Zheng and S.-Z. Qiao, *Sci. Adv.*, 2022, **8**, eabo0762.
38 M. M. J. Smulders, M. M. L. Nieuwenhuizen, T. F. A. de Greef, P. van der Schoot, A. P. H. Schenning and E. W. Meijer, *Chem. – Eur. J.*, 2010, **16**, 362–367.
39 D. Zhao and J. S. Moore, *Org. Biomol. Chem.*, 2003, **1**, 3471–3491.
40 T. F. A. De Greef, M. M. J. Smulders, M. Wolffs, A. P. H. Schenning, R. P. Sijbesma and E. W. Meijer, *Chem. Rev.*, 2009, **109**, 5687–5754.
41 T. Lu and F. Chen, *J. Comput. Chem.*, 2012, **33**, 580–592.

 